Available online at www.sciencedirect.com
SCIENCE DIRECT®
Acta Materialia 52 (2004) 57–68
Acta MATERIALIA
www.actamat-journals.com

The role of plastic deformation of rough surfaces in the size-dependent hardness

Tong-Yi Zhang *, Wei-Hua Xu, Ming-Hao Zhao

Department of Mechanical Engineering, Hong Kong University of Science and Technology, Clear Water Bay, Kowloon, Hong Kong, China

Received 28 May 2003; received in revised form 20 August 2003; accepted 23 August 2003

Abstract

In this study, we propose a bearing ratio model for nanoindentation of rough surfaces. During an indentation test, the work done by an applied indentation load contains the bulk work and the surface work. The surface work causes plastic deformation of an indented rough surface and thus dissipates energy, which is necessary to form an impression on a solid. The energy dissipation occurring at the indented surface is among the factors that cause the Indentation Size Effect (ISE) at the micro/nanometer scales. In particular, the surface effect predominates when the indentation depth is shallow. Good agreement is found between the theoretical and experimental results of the size-dependent hardness, indicating that the surface effect plays an important role in size-dependent hardness.

Keywords: Nanoindentation; Hardness; Surface energy; Micro/Nanomechanical modeling

1. Introduction

Since the beginning of the last century, indentation tests have been widely used to characterize the mechanical properties of materials [1,2]. The development of microindentation [3,4] and instrumented nanoindentation techniques [5–7] enables us to investigate the material properties at the micro/nanometer scales. There are many reports in the literature on how to extract information on the material properties from the instrumented indentation tests [8–12]. At the micro/nanometer scales, the hardness depends on the indentation depth or load, exhibiting the well-known Indentation Size Effect (ISE). A decrease in the hardness with increasing indentation depth or load has been observed in numerous micro/nanoindentation tests on various materials such as metals, diamond-like carbon, polymers, ceramics, etc. [3,5,13–20], which may be called the normal ISE. The inverse ISE has also been reported, in which the hardness increases with increasing indentation depth or load [21–24]. Although there are many mechanisms causing the ISE [25–27], the dislocation plasticity theory and the surface effects are two major mechanisms of interest.

The ISE in crystalline materials can be explained on the basis of the concept of geometrically necessary dislocations [28]. In 1993, Stelmashenko et al. [29] studied the ISE on the (1 0 0), (1 1 0) and (1 1 1) surfaces of Mo and W single crystals and proposed a reasonable explanation in terms of the local dislocation hardening due to geometrically necessary dislocations. For W single crystals, when the indentation depth is less than 500 nm, the (1 0 0) nanohardness is the highest, the (1 1 0) nanohardness is in the middle and the (1 1 1) nanohardness is the lowest. The hardness, H, is given by

$$H = A\alpha\mu b\left(\rho_0 + \frac{\cot\beta}{bd}\right)^{1/2}, \tag{1}$$

where the constant A is the ratio of the average normal pressure to the flow stress and is about 3 for metals and 1.5 for glass [30–32], the constant α is normally taken to be 1/3, μ is the shear modulus, b is the Burger's vector, ρ_0 is the background dislocation density or a dislocation density appropriate to a representative strain, $\cot\beta$ is the wedge shape of an indenter ($\beta = 136°$ for a Vickers indenter), and d is the diagonal of the impression.

* Corresponding author. Tel.: +852-235-87192; fax: +852-235-81543.
E-mail address: mezhangt@ust.hk (T.-Y. Zhang).

1359-6454/$30.00 © 2003 Acta Materialia Inc. Published by Elsevier Ltd. All rights reserved.
doi:10.1016/j.actamat.2003.08.026

Stelmashenko et al. [29] let the value of $A\alpha$ vary from 2 to 3 for different crystalline surfaces to explain the observed change in hardness with the crystalline orientation. Eq. (1) is fundamental to understanding ISE hardness based on the dislocation theory. In 2002, Gerberich et al. [33] found that, for W single crystals, Eq. (1) with a reasonable value of $A\alpha \approx 1.5$ fits satisfactorily with the data for Vickers tips [29] and with the other ISE data for spherical tips ranging from 85 to 5000 nm in radius [34,35].

In 1995, Ma and Clark [17] suggested that the density of geometrically necessary dislocations, ρ_G, is related to the strain gradient by compatibility requirements. They estimated the strain gradient by the average shear strain, γ, underneath the impression divided by the impression diameter, D, i.e., $\rho_G \approx 4\gamma/(bD)$. Following Taylor's dislocation work hardening theory that the flow stress is proportional to the square root of the total dislocation density, Ma and Clark divided the total dislocation density into the geometrically necessary dislocation density, ρ_G, and the statistically stored dislocation density, ρ_S. Then, Ma and Clark [17] proposed a simplified strain gradient plasticity model for the size-dependent hardness. When replacing ρ_0 and $\cot\beta/(bd)$ in Eq. (1) by ρ_S and $4\gamma/(bD)$, respectively, one should have the size-dependent hardness proposed by Ma and Clark [17]. The simplified strain gradient plasticity model fits excellently with the experimentally measured data of silver single crystals indented with a Berkovich indenter. In addition to the simplified strain gradient plasticity model, Ma and Clark [17] also developed a geometrical scaling model for the ISE. They partitioned the applied indentation force into the force on the flat surfaces and the force over the edges and derived the size-dependent hardness for various indentation tips:

$$H = H_0 + \hat{\beta}\frac{8\sqrt{3}}{3D^2}\left[\left(1+\sqrt{3}\right)D - \hat{d}\right] \quad \text{for Berkovich indenters,} \tag{2a}$$

$$H = H_0 + \hat{\beta}\frac{4}{D^2}\left[\left(1+\sqrt{2}\right)D - \hat{d}\right] \quad \text{for Vickers indenters,} \tag{2b}$$

$$H = H_0 + \hat{\beta}\frac{4}{D} \quad \text{for conical and hemispherical indenters,} \tag{2c}$$

where H_0 represents the macroscopic hardness and all constants, H_0, $\hat{\beta}$ and $\hat{d}$, are determined by the best fit to the experimental data. Clearly, the mathematic format of Eqs. (2a)–(2c) is completely different from the mathematic format of Eq. (1). However, the fitting of Eq. (2a) to the size-dependent hardness of silver is as perfect as the fitting of the simplified strain gradient plasticity model, thereby indicating that a set of experimental data can be almost equally well fitted with different equations.

Nix and Gao [25] clearly showed that the ISE for crystalline materials could be modeled using the concept of geometrically necessary dislocations and Taylor's dislocation work hardening theory. For a geometric self-similar indenter, the size-dependent hardness, in terms of the indentation depth, h, is given by

$$H = H_0\sqrt{1 + h^*/h}, \tag{3}$$

where h^* is a characteristic length that depends on the indenter shape, Burger's vector and the statistically stored dislocation density. In practice, H_0 and h^* are treated as fitting parameters. Eq. (3) fits the depth-dependent hardness of (1 1 1) single crystal Cu, cold worked polycrystalline Cu, (1 0 0) and (1 1 0) single crystal Ag well when the data for depths less than 100 nm are excluded because the shape of the indenter is not self similar at small indentation depths. Using this model, Nix and Gao developed a law for strain gradient plasticity, which became the theoretical basis of the mechanism-based strain gradient plasticity.

Swadener et al. [36] extended Nix and Gao's model to the case of spherical indenters. Their analytic results indicate that, for a spherical indenter, the hardness is not dependent on depth, but depends on the radius of the indenter, R. Correspondingly replacing h^* and h in Eq. (3) with R^* and R gives the radius-dependent hardness, $H = H_0\sqrt{1 + R^*/R}$, for spherical indenters. In addition, Swadener et al. [36] studied the correlation of the ISE determined with spherical and pyramidal indenters by equaling the geometrically necessary dislocations required by each indenter, which yields $R^* = 5.2h^*$. Xue et al. [37] also studied the ISE for spherical indenters by using the theory of mechanism-based strain gradient plasticity. Their results show that, for a given contact radius, the calculated hardness increases as the tip radius decreases. For a given tip radius, however, the calculated hardness increases as the contact radius increases, exhibiting inverse ISE, which differs from the results obtained by Swadener et al. [36].

As more and more experimental results are reported, researchers find that Eq. (3) cannot accurately fit all the experimental results. Therefore, Eq. (3) has been modified within the scheme of dislocation plasticity theory. Swadener et al. [38] added a contact-depth-independent constant, H_1, to the right-hand term of Eq. (3), i.e., $H = H_0\sqrt{1 + h^*/h} + H_1$, where H_1 is a work hardening component representing increases in hardness from the onset of yielding to an effective strain. The modified equation was then used to study the ISE in a (1 0 0) NaCl single crystal and a (1 0 0) LiF single crystal. Elmustafa and Stone [39,40] studied the ISE using combined micro/nanoindentation tests on highly pure Al and alpha brass samples. They added a contact-depth-independent constant, H_f, which is similar to the work hardening component, H_1, to the right-hand term of Eq. (3). The hardness, H_f, represents the contribution of

hardening mechanisms other than dislocations. When using the modified equation to fit the experimental data, they found that, for depths shallower than 150 nm, the slope decreased abruptly by a factor of 10 in comparison with the microhardness and deep nanoindentation data. Qiu et al. [41] considered the intrinsic lattice resistance, σ_0, which varies with the lattice orientation, and modified Eq. (3) to

$$H = 3\sigma_0 + H_0\sqrt{(1-3\sigma_0/H_0)^2 + h^*/h} = H_1^* + H_0^*\sqrt{1+h^{**}/h},$$

where $H_0^* = H_0/(1-3\sigma_0/H_0)$, $H_1^* = 3\sigma_0$, and $h^{**} = h^*/(1-3\sigma_0/H_0)^2$ are all depth-independent. The modified formula has a similar form as that proposed by Swadener et al. [38] and Elmustafa and Stone [39,40]. With the modified model, Qiu et al. [41] explained the dependence of ISE on the crystalline orientation, which was observed in W crystals [29]. In summary, the above discussions indicate that different models may result in an apparently identical ISE formula.

There is much less theoretical work on the mechanisms of the ISE of polymers in the literature. Lam and Chong [42], by following the molecular theory of yield for glassy polymers, proposed a size-dependent hardness for polymers

$$H = H_0\left(1+\sqrt{h^*/h}\right). \tag{4}$$

Eq. (4) was verified by experimental results on epoxy resin and polycrabonate [43].

Another mechanism of the ISE is the surface effect. An illustrative example of the surface effect may be attributed to an oxidation or work-hardened layer. An oxidation layer, thick or thin, always exists at the surface of a metallic sample in the conventional testing environment and a work-hardened layer at the surface of a sample can be formed during the sample preparation, especially by mechanical machining and mechanical polishing. The oxidation layer or the work-hardened layer could be much harder than the bulk material so that the sample is harder when the indentation depth is shallow because the indenter is mainly in contact with the oxidation layer or the work-hardened layer [44]. Liu and Ngan [45] observed that at the same contact depth, a mechanically polished (1 1 1) Cu crystal is harder than an electromechanically polished (1 1 1) Cu crystal. They attributed this phenomenon to a work-hardened thin layer formed on the mechanically polished sample.

Gerberich et al. [33] proposed that the ISE should be linked to a ratio between the energy of the newly created surface and the plastic strain energy dissipation. They estimated the surface work and the volume work associated with the plastic deformation during an indentation test. There are a number of possible contributions to the indentation surface work as follows: (1) creating a new surface associated with straining material outside the contact, (2) creating a surface by fracture of oxide, if any, or by fracture of the metal/oxide interface, (3) adhesion between the indenter-tip and the indented material, and (4) surface stress deformation work outside the area of contact. Their analysis indicates that, in the first-order approximation, the total surface work is given by the product of the contact area and the surface energy. They found that the contact-surface-to-plastic-volume ratio was nearly constant for a range of shallow depths and the ratio of the surface work to the plastic volume work decreases rapidly with increasing depth of penetration, thereby leading to the ISE. They gave the size-dependent hardness,

$$H \cong \frac{\sigma_f}{(S/V)^{2/3}}\cdot\frac{1}{(3hR)^{1/3}}, \tag{5}$$

where σ_f is an appropriate flow stress and S/V denotes the ratio of the contact surface to the plastic volume. Eq. (5) fits the size-dependent data in the (1 0 0) W, (1 0 0) Fe–3 wt%Si, (1 0 0) Au, and (1 0 0) Al single crystals for a large range of tip radii from 70 to 20,000 nm. It may be interesting to note that their experimental results with spherical tips reveal the normal ISE, which differs from the theoretical predictions by Swadener et al. [38] and Xue et al. [37], thereby indicating that other mechanisms rather than strain gradient plasticity may predominate in Gerberich et al.'s [33] tests.

Zhang and Xu [26] studied the surface effect on nanoindentation and introduced an apparent surface stress that represents the energy dissipated per unit area of a solid surface in a nanoindentation test. They analyzed the work done by an applied indentation load that contains both bulk and surface work. Surface work, which is related to the apparent surface stress and the size and geometry of an indenter tip, is necessary in the deformation of a solid surface. The size-dependent hardness is given by

$$H = H_0\sqrt{1+\frac{h^*}{h}} + g\frac{f}{h} \quad \text{for crystalline materials,} \tag{6a}$$

$$H = H_0\left(1+\sqrt{\frac{h^*}{h}}\right) + g\frac{f}{h} \quad \text{for polymeric materials,} \tag{6b}$$

where g is a numerical factor of $2\sqrt{3}$, 1.1827 and 2.2406 for Northstar, Berkovich, and Vickers tips, respectively, and f denotes the apparent surface stress. The second term on the right-hand side of Eq. (6), gf/h, represents the surface contribution to the ISE, while the term $\sqrt{1+h^*/h}-1$ or $\sqrt{h^*/h}$ stands for the bulk contribution to the ISE. Without including the bulk contribution, Zhang and Xu [26] fit their experimental data and the experimental data reported in the literature for metals, diamond-like carbon, polymers, and ceramics

with $H = H_0 + gf/h$. Good agreement was found between theoretical first-order approximations and empirical data on depth-dependent hardness, indicating that the apparent surface stress plays an important role in depth-dependent hardness. This good fit is surprising because depth-dependent hardness also fits well with the formula, $H = H_0\sqrt{1 + h^*/h}$, for metals and with the formula, $H = H_0(1 + \sqrt{h^*/h})$, for polymers. This means that the experimental data on depth-dependent hardness can fit with different formulas derived from different models. Ma and Clark [17] have found, as mentioned above, the similar phenomenon that a set of experimental data could be fitted with different formulas. In addition, Zhang and Xu [26] introduced a critical indentation depth, h_c. The surface deformation predominates if the indentation depth is shallower than the critical depth, while the bulk deformation predominates when the indentation depth is deeper than the critical depth. However, the apparent surface stress extracted from the nanoindentation test is about two or three orders higher in magnitude than the surface energy of the same material. Zhang and Xu [26] attributed the high values of apparent surface stress to friction and/or plastic deformation occurring at the contact surface. But they did not explore the mechanism of the high apparent surface stress.

Actually, many researchers [22,46–52] have studied the surface term in Eq. (6) without including the bulk contribution, i.e., the hardness formula of $H = H_0 + C/h$, where C is a constant. Bernhardt [47] and Fröhlich et al. [48] related the surface term to the energy consumed in creating new surfaces of indentation facets and microcracks. Hirao and Tomozawa [49] tried to correlate this term to the surface energy and found that the evaluated surface energies of silica, borosilicate, and soda-lime ceramics were extremely large, with the magnitude on the order of 10^4 J/m^2. Li et al. [22] attributed the surface term to frictional and elastic contributions. Swain and Witting [50] believed that the surface term was created by the median cracks under the Knoop indentations. By numerical simulations, Bobji and Biswas [51] demonstrated that surface roughness has a substantial influence on nanohardness, irrespective of whether the bulk and surface mechanical properties are the same. Gao and Fan [52] connected the surface term to the plastic energy dissipated at an indented rough surface. Following the elastic–plastic model for the contact of rough surfaces proposed by Chang et al. [53], Gao and Fan [52] conducted a plastic deformation analysis of asperities of a rough surface with the basic assumptions in Chang et al.'s model that asperities are spherical near their summits with all having the same radius, R_{asp}, and that there is no deformation in the bulk and no interaction between asperities such that only individual asperities deform during contact. Using an exponential distribution of summits, Gao and Fan [52] estimated the apparent surface energy, which they called the dissipation energy per contact area, e_c:

$$e_c = \pi p_0 \eta R_{asp} \sigma (2\sigma + \omega_c) \exp(-\omega_c/\sigma), \tag{7}$$

where p_0 is the flow pressure, η is the asperity density, σ is the standard deviation of the summit distribution, and $\varpi_c = R_{asp}(\pi p_0/2E)^2$ is the critical interference with E being Young's modulus. Since so many parameters are involved in e_c, it must be very challenging to verify Eq. (7) experimentally. Nevertheless, the merit of Eq. (7) lies in that it links the apparent surface energy to the plastic work required to deform a rough surface.

In the present work, we develop a nanomechanics model to predict the apparent surface stress of a rough indented surface. Chang et al.'s model [53] is appropriate for a range of moderately loaded contacts where the asperity deformations are primarily elastic but where there is also an appreciable percentage of asperities beyond their elastic limit. We believe, however, that, during a nanoindentation test, asperities on an indented rough surface must all be plastically deformed. The peaks of the asperities flow plastically down to fill up the valleys of the rough indented surface such that the residual contact surface will become microscopically flat and insensitive to the original roughness, thereby causing the pull-out force to be insensitive to the original roughness. Our nanomechanics model is based on severe plastic deformation and a directly measurable parameter, the bearing ratio, of a rough surface. The experimental results of instrumented nanoindentation tests on metallic and polymeric samples with different rough surfaces verify our nanomechanics model.

2. Analysis

2.1. Hardness

Following Zhang and Xu's approach [26], we analyze the work done by an applied load in a nanoindentation test. During an infinitesimal increase in the indentation depth, δh, under an indentation load, P, the work done by the indentation load,$P\delta h$, can be divided into the bulk work, δE_b, causing deformation of the bulk material and the dissipated energy, δE_s, at the surface layer of the indented sample, i.e.,

$$P\delta h = \delta E_b + \delta E_s. \tag{8}$$

The elastic deformation energy in the system is released during the unloading process, so no term for the elastic energy change is included in Eq. (8). The surface dissipation energy can be further divided into two terms

$$\delta E_s = e_c \delta A_p + f_s \delta A_c, \tag{9}$$

where A_p and A_c are the contact project area and the contact area, respectively, as shown in Fig. 1, f_s is the

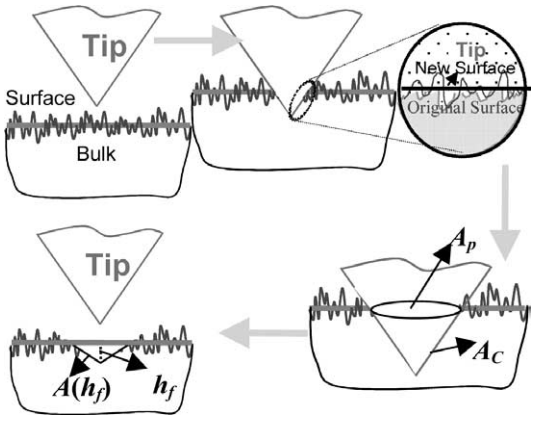

Fig. 1. A schematic of nanoindentation processing, where A_p, A_c, h_f, and $A(h_f)$ denote the project area, contact area, residual depth and residual area, respectively. An indented material can be divided into the surface layer and the bulk region. The rough surface layer must be deformed prior to deforming the underneath bulk. The surface deformation makes the residual contact surface flat.

thermodynamic surface stress and e_c is the dissipation energy per contact project area due to the plastic deformation occurring at the indented surface, which is also called the surface contact dissipation energy density. In addition to the surface energy term, $f_s\delta A_c$, which is consistent with the analysis of Gerberich et al. [33], Eq. (9) includes the surface plastic work, $e_c\delta A_p$. Note that Gao and Fan [52] defined e_c as the dissipation energy per contact area rather than per contact project area. We believe that the contact project area possesses the original surface morphology and the contact area has a different surface morphology due to plastic deformation. Eq. (9) shows that the surface dissipation energy is generated by increases in both the surface energy and the surface plastic work.

For a material with a perfectly flat surface, the bulk energy can be easily calculated by the hardness without including any surface effects, because the hardness is usually defined as the mean pressure on the indentation-projected contact area. For example, if the hardness expression proposed by Nix and Gao [25] is used, the bulk energy can be obtained by

$$\delta E_b = \sqrt{1+\frac{h^*}{h}}H_0A_p\delta h. \tag{10}$$

Substituting Eqs. (9) and (10) into Eq. (8) yields

$$P = \sqrt{1+\frac{h^*}{h}}H_0A_p + e_c\frac{\delta A_p}{\delta h} + f_s\frac{\delta A_c}{\delta h}. \tag{11}$$

Then, dividing the two sides of Eq. (11) by A_p and taking into account the indenter tip geometry, we have the hardness

$$H = H_0\sqrt{1+\frac{h^*}{h}} + \frac{F}{h}, \tag{12}$$

with

$$F = 2e_c + gf_s, \tag{13}$$

where g is the geometric constant, as described above, and the factor 2 is derived from the geometric self-similarity of the indenter tips. Eq. (12) is identical to Eq. (6a) if we define the apparent surface stress as

$$f = 2e_c/g + f_s. \tag{14}$$

Similarly, we have the hardness given by Eq. (6b) for polymers with the apparent surface stress defined by Eq. (14). In general, the apparent surface stress should be a function of the indentation depth. To demonstrate the surface effect, we simply take it as a constant in the first step approximation. Thus, for a given indenter shape and tested material, F is a constant and independent of the indentation depth, which allows us to extract its value from the nanoindentation tests.

2.2. The dissipation energy per contact project area, e_c, for a rough surface

In 1933, Abbott and Firestone [54] proposed a surface microgeometry model for plastic contact in which the deformation of a rough surface against a rigid flat plate is equivalent to the truncation of the undeformed rough surface at its intersection with the flat plate. The area of contact is simply the geometrical intersection of the flat plate with the original profile of the rough surface, and the pressure over the contact is the flow pressure. The surface microgeometry model, however, did not taken the volume conservation of plastic deformation into account. In 1972, Pullen and Williason [55] developed a plastic contact model of rough surfaces, which is called the PW model in the present work. The PW model is based on three physical observations: that the total volume of the material is not changed by plastic deformation; that the mean indentation pressure is a well-defined material constant applicable to the whole range of likely asperity shapes; and that the displaced material reappears as a uniform rise in the non-contacting surface. Our nanomechanics model is a direct consequence and further development of the PW model. We believe that, in a nanoindentation test, asperities on an indented rough surface must all be plastically deformed. In the nanomechanics model, we assume that perfect plasticity is applied to all asperities with the same flow pressure. Furthermore, the contact project area is assumed to be much larger than the size of each individual asperity and the material volume does not change during the plastic deformation. Thus, the peaks of the asperities flow plastically down to fill up the valleys of the rough indented surface, from which the surface plastic work per project area is defined as

$$e_c = p_0V_p \quad \text{with } V_p = \int_{d_m}^{d_{max}} t_p(d)\,\mathrm{d}d, \tag{15}$$

where p_0 is the plastic flow pressure of the material and t_p is the bearing ratio, which is defined as the total interception area when a horizontal plane slices through a rough surface parallel to the mean plane. Experimentally, the bearing ratio is determined by $t_p = (1/A)\sum_{i=1} a_i$, where a_i is the area of individual asperities at height d and A is the nominal surface area examined. The integration limits, d_m, d_{min} and d_{max}, in Eq. (15) denote the mean, minimum and the maximum heights, respectively, as illustrated in Fig. 2. V_p represents the average peak volume of asperities per unit nominal surface area that is moved to fill up the valleys. Since the present model is based on the bearing ratio, we may call it the *bearing ratio model* for nanoindentation of rough surfaces. Comparing Eq. (15) with Eq. (7) shows the obvious difference in the surface plastic work per project area derived from the two models.

2.3. Thermodynamic surface stress

In the present work, the thermodynamic surface stress, f_s, is estimated by the work of adhesion, γ, i.e., $f_s \approx \gamma$. The nanoindentaion tests reveal the pull-off phenomenon. From the pull-off force, F_p, we can determine the work of adhesion, $\gamma = \gamma_1 + \gamma_2 - \gamma_{12}$, where γ_1 and γ_2 are the surface energies of the indenter tip and the indented material, respectively, and γ_{12} is the interface energy between the indenter tip and the indented material. The atomic interaction of the surface adhesion is usually described by the Lennard–Jones potential. In an elastic–plastic sample, the pull-off force is directly proportional to the residual contact area, i.e., $F_p = -KA_f$, when the DMT model [56] is adopted, where A_f denotes the residual contact area and K is a proportionality constant in units of N/m^2. If we take the Dugdale approximation for the surface force potential, we have $K = 1.03\gamma/z_0$, where z_0 is the equilibrium separation [57]. Therefore, the work of adhesion is determined from

$$\gamma = -\frac{F_p z_0}{1.03 A_f}. \tag{16}$$

In the nanoindentation tests based on Oliver and Pharr's method [6], the project contact area used to determine the hardness is calibrated as a function of the contact depth before unloading. The calibrated area function is adopted here to calculate the residual contact area from the residual depth, h_f, as shown in Fig. 1. The residual depth can be directly measured during the tests.

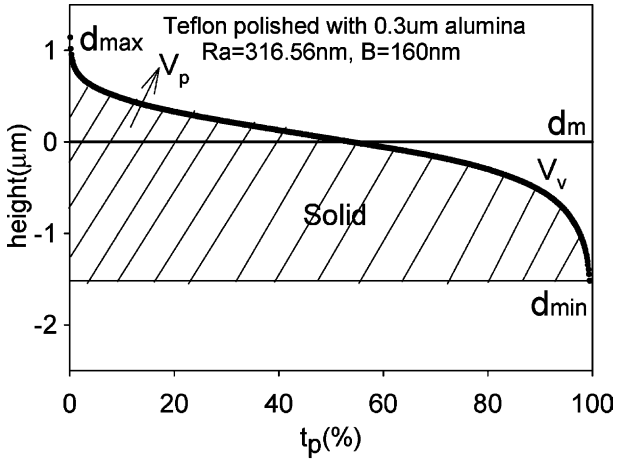

Fig. 2. A typical bearing ratio curve, where V_p and V_v denote the volumes of the peaks and valleys of a rough surface and $V_p = V_v$. During the nanoindentation tests, the material in the peak volume plastically flows to fill up the volume of valleys.

3. Experiments

To demonstrate the roughness effect in the depth-dependent hardness and to verify the proposed bearing ratio model, nanoindentation tests were conducted on 63Sn–37Pb alloys and Teflon with different surface roughnesses.

The Sn–Pb alloys were melted at 200 °C and then poured on a clean four-inch silicon wafer, which functioned as a solid holder. The Sn–Pb sample surface was ground with sand paper down to 600-grit to make the sample surface parallel to the bottom of the silicon holder. Then, the sample surface was further mechanically polished with 3 μm alumina suspension. After that, a small piece of sample (10 mm × 5 mm × 3 mm) was cut from the big sample. The rest of the big sample was further mechanically polished with 1 μm alumina suspension. After the polishing, two small pieces of the samples (10 mm × 5 mm × 3 mm) were cut away. One of the two samples was further polished for more than 30 min using 0.05 μm colloidal Alumina on a GAMMA micropolish^R, followed by supersonic cleaning in ethanol and distilled water. To remove any potential residual stresses caused by the mechanical polishing, the three Sn–Pb samples were annealed at 150 °C for 60 min. After the annealing, X-ray diffraction (Model PW1825, Philips) was used to measure the potential residual stresses on the Sn–Pb sample surfaces.

Three samples were cut from a big piece of Teflon (PTFE) polymer. The three samples were polished for 60 min with the sand paper with 9, 3, and 0.3 μm alumina, respectively. All the Teflon samples were annealed at 130 °C for 60 min to remove any potential surface residual stresses induced by the mechanical polishing. Then, Raman spectroscopy was conducted with a Micro-Raman/Photoluminescence System (Renishaw, model 3000). An argon ion laser beam with a 633-nm wavelength with a power of 5 mW was used in the Raman spectroscopy tests. The Raman spectroscope was calibrated and checked using a standard silicon sample before and after recording the Raman spectra from the Teflon samples.

A Wyko NT 3300 optical profiler was used to measure the roughness parameter, R_a, and the bearing ratio, t_p, of the samples. Each measurement was made over a nominal area of 62 μm × 81 μm and the measurements were made at 20 locations of each sample. The mean values of the roughness parameter and the bearing ratio are listed in Table 1 with their corresponding standard deviations.

The nanoindentation tests were conducted by using a Hysitron nanomechanical test system with a Berkovich diamond indenter. Oliver and Pharr's method [6] was adopted in the present study to determine the hardness. The Hysitron nanomechanical test system had an atomic force microscopy mode, which allowed us to image the impression after each nanoindentation test. The indentation loading and unloading rates were the same at 150 μN/s. The separation between two adjacent testing points was 60 μm, which was sufficiently large that each indentation test could be treated as an individual event. The range of indentation loads was set from 0.2 to 9.9 mN for both the Teflon and Sn–Pd samples, which yielded indentation contact depths ranging from about 10 to about 450 nm for the Teflon samples and from about 5 to about 1500 nm for the Sn–Pd samples. Before and after the tests, the nanoindentation system was calibrated by using a standard sample of fused quartz.

4. Results and discussion

4.1. Surface morphology and residual surface stresses

Fig. 3 shows typical surface morphologies for the Teflon samples, while Fig. 4 illustrates typical surface morphologies for the Sn–Pb samples. The measured roughness means with standard deviations are listed in Table 1. As mentioned by Johnson [30], a less common but statistically more meaningful measure of average roughness is the standard deviation, σ, of the height distribution. The relationship between the roughness and the standard deviation depends on the nature of a rough surface, for instance, $\sigma = R_a\sqrt{\pi/2}$ for a normal distribution of heights. When a probability function is used to describe the height distribution, the bearing ratio represents its cumulative probability function. From the directly measured bearing ratio, we calculate the average peak volume per unit of nominal surface area, V_p and tabulate the results in Table 1. In general, the higher the value of the roughness, the larger the value of V_p is, as indicated in Table 1. Theoretically, if the probability function of surface heights is available, we are able to calculate the value of V_p. For example, if surface heights follow a normal distribution, the average peak volume per unit of nominal surface area, V_p, is calculated by

$$V_p = \int_{-\infty}^{0}\left[\frac{1}{\sqrt{2\pi}\sigma}\int_{-\infty}^{x}\exp\left(-\frac{y^2}{2\sigma^2}\right)dy\right]dx = 0.3989\sigma = 0.5R_a. \quad (17)$$

The experimental data listed in Table 1 show that, for the Teflon samples, the ratio of V_p/R_a is almost exactly 0.5, thereby indicating that the heights follow the normal distribution. For the Sn–Pd samples, however, the ratios of V_p/R_a are 0.54, 0.60 and 0.57 for the samples polished with 3, 1 and 0.05 μm alumina, respectively. The deviation from 0.5 implies that the heights do not exactly follow the normal distribution in the Sn–Pd samples, as indicated in Fig. 5.

Fig. 6 shows the Raman spectra of the Teflon samples after mechanically being polished with 9 μm, 3 μm and 0.3 μm alumina respectively, and then annealed at 130 °C for 60 minutes. Raman spectroscopy was used to detect the potential surface stresses [58]. Compared with the

Table 1
Experimental and calculation results

	Sn–Pb alloys			Teflon polymers		
	With 3 μm alumina	With 1 μm alumina	With 0.05 μm alumina	With 9 μm alumina	With 3 μm alumina	With 0.3 μm alumina
R_a (nm)	237 ± 73	122 ± 24	97 ± 21	482 ± 70	397 ± 64	293 ± 90
V_p (nm)	129 ± 38	73 ± 14	55 ± 11	241 ± 35	197 ± 32	147 ± 44
V_p/R_a	0.54	0.60	0.57	0.50	0.50	0.50
h^* (nm)	101	144	227	203	19	18
H_0 (MPa)	221	215	191	24	41	44
	Mean: 209			Mean: 36		
γ (mJ/m^2)	7.7	14.4	9.5	8.0	8.9	11.5
	Mean: 10.5			Mean: 9.5		
F (J/m^2)	14.72	8.75	5.90	4.16	2.40	1.90
h_c (nm)	137	27	6	144	181	109
e_c (J/m^2)	7.36	4.37	2.94	2.08	1.19	0.94
f (J/m^2)	12.43	7.37	4.97	3.50	2.01	1.59
$e_c/(V_pH_0)$	0.26	0.28	0.28	0.35	0.15	0.15
	Mean: 0.27			Mean: 0.22		

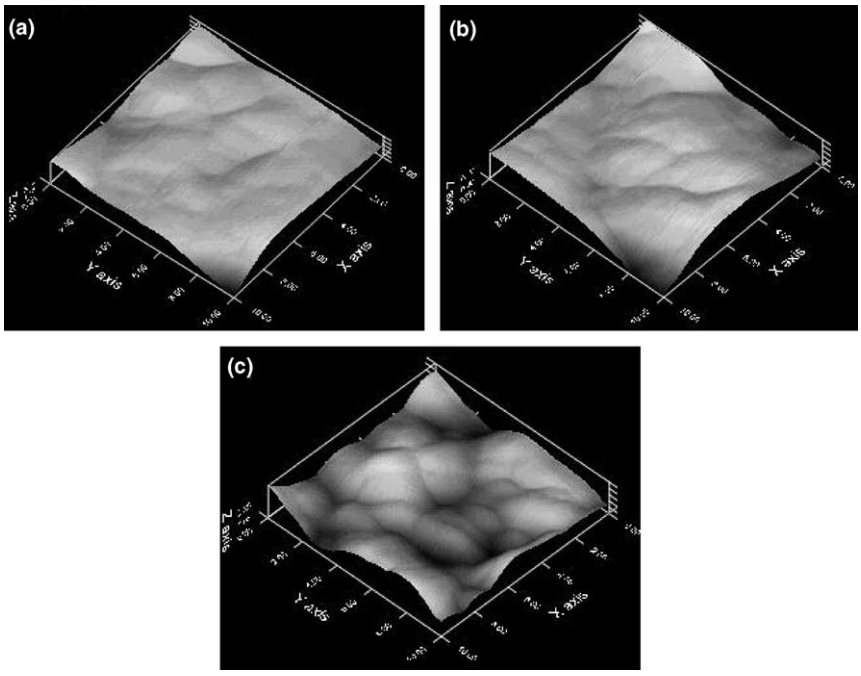

Fig. 3. In situ AFM surface 3D morphologies (10 μm × 10 μm) of Teflon samples mechanically polished with (a) with 0.3 μm alumina, (b) 3 μm alumina, and (c) 9 μm alumina.

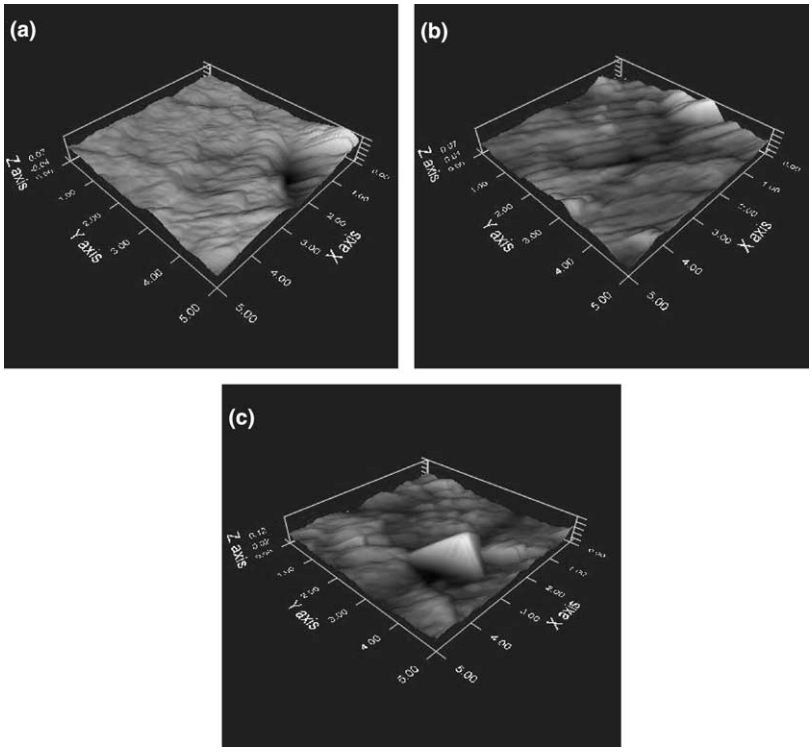

Fig. 4. In situ AFM surface 3D morphologies (5 μm × 5 μm) of Sn–Pb samples mechanically polished with (a) with 0.05 μm alumina, (b) 1 μm alumina, and (c) 3 μm alumina.

standard Raman spectra, we did not find any changes. The experimental results indicate no detectable residual stresses at the surfaces. Fig. 7 illustrates the experimental results of the X-ray diffraction $\sin^2\psi$ measurements on the Sn–Pd sample. The measured residual stresses are 18.2 ± 23.1, -4.2 ± 6.5, and 10.0 ± 11.1 MPa

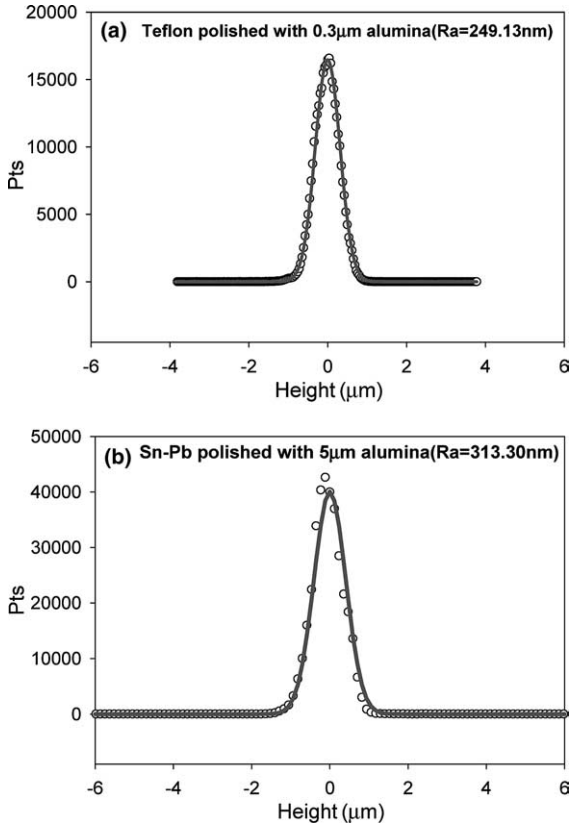

Fig. 5. The height distributions in (a) a Teflon sample and (b) a Sn–Pd sample, where the solid curves are plotted according to the normal distribution. The heights of the Teflon sample follow the normal distribution, whereas the heights of the Sn–Pd sample deviate to some extent from the normal distribution.

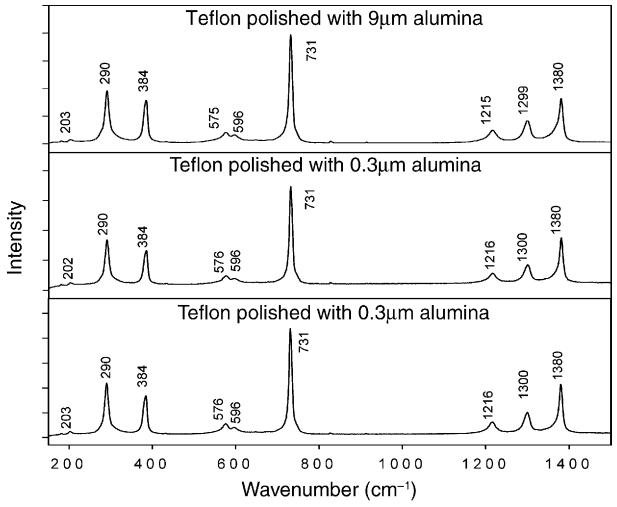

Fig. 6. The Raman spectra of the Teflon samples after mechanically being polished with 9, 3, and 0.3 μm alumina, respectively, and then annealed at 130 °C for 60 min.

in the Sn–Pb samples mechanically polished with 0.05, 1, and 3 μm alumina, respectively. The stress measurements indicate that the average values are small and

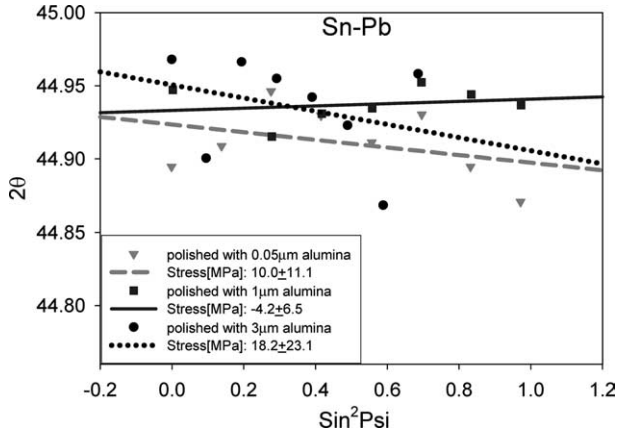

Fig. 7. The experimental results of the X-ray diffraction $\sin^2\psi$ measurements on the Sn–Pd samples after being polished with 0.05, 1, and 3 μm alumina, respectively, and then annealed at 150 °C for 60 min.

change from positive to negative and the standard deviations are large.

4.2. Hardness

Fig. 8 illustrates hardness as a function of the indentation depth for all the indentation depths, while the inset figures show the hardness as a function of the reciprocal indentation depth for depths less than 150 nm. There are three parameters in Eq. (6a) or Eq. (6b) that have to be extracted from the relationship between hardness and indentation depth. In the fitting process, we find that the three parameters cannot be uniquely determined by only minimizing the fitting error. Since the surface term predominates when the depths are shallower than a critical value, we fit the value of F first with shallow depths less than 150 nm, which is shown in the inset figures. The plots in the insets reveal that there is a linear relationship between the hardness and the reciprocal indentation depth for a given surface roughness if the depths are shallower than 150 nm. From the linear regression of the experimental data, we determine the value of F for each given surface roughness and tabulate the results in Table 1. The results indicate that, for a given material, the rougher the surface, the higher the value of F is. With the evaluated F, we then use Eq. (6) to determine the values of H_0 and h^* for each sample. Since the value of the macrohardness, H_0, should be the same for a given material and independent of the surface roughness, the mean of three initial fitted values of H_0 is used to fit the value of h^*. In Table 1, we tabulate all the fitting results of F, H_0, and h^*. The results indicate that, for the Sn–Pd samples, the rougher the surface, the lower the value of h^* is. This may be attributed to the surface step effects on nanoindentation [10,59]. There may be more surface steps on a rougher surface and thus the dislocation emission is much easier.

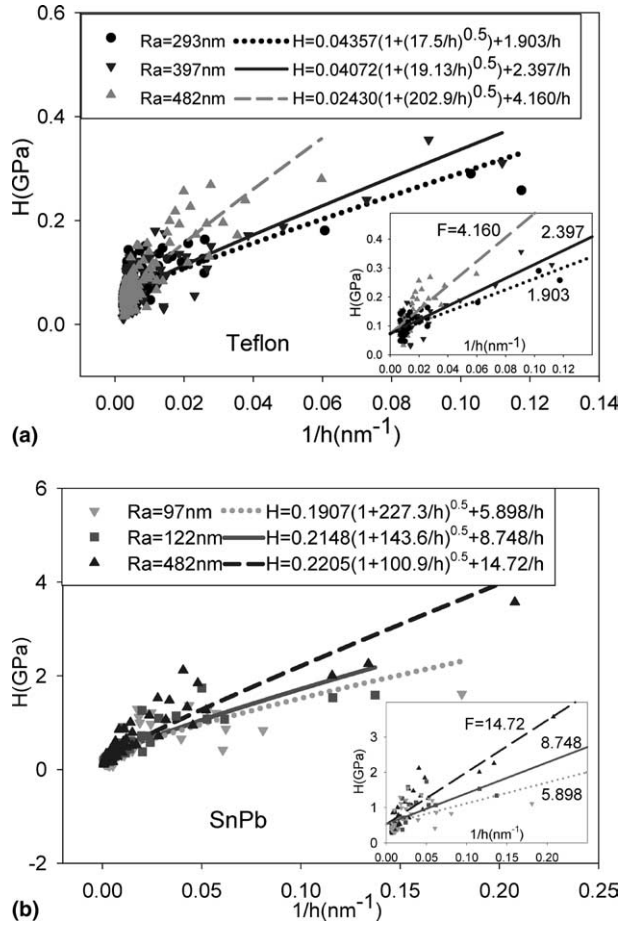

Fig. 8. The hardness as a function of the indentation depth (a) for the Teflon samples and (b) for the Sb–Pd samples, where the inset figures show the hardness as a linear function of the reciprocal indentation depth for shallow depths less than 150 nm. From the linear regression, we determine the value of F and then extract the values of H_0 and h^* by fitting experimental data of the entire range of depths with Eq. (6).

4.3. Adhesion

We plot the pull-out force extracted from the unloading curves as a function of the residual contact area in Fig. 9. The plots illustrate that the pull-out force is approximately a linear function of the residual contact area. The linear relationship between the pull-out force and the residual contact area is independent of the initial surface roughness, as shown in Fig. 9. This is because the plastic deformation makes the final surface morphology of the contact area almost the same. As described above, the original peaks of the asperities plastically flow down to fill up the original valleys, which leads to the residual contact area becoming independent of the original surface roughness. With Eq. (16), we estimate the work of adhesion with the equilibrium separation of 0.5 nm and list the result in Table 1 as well. The mean values of the work of adhesion are 10.5 and 9.5 mJ/m^2 for the Sn–Pb and the Teflon samples, respectively, which are consistent with the data reported in the literature [60].

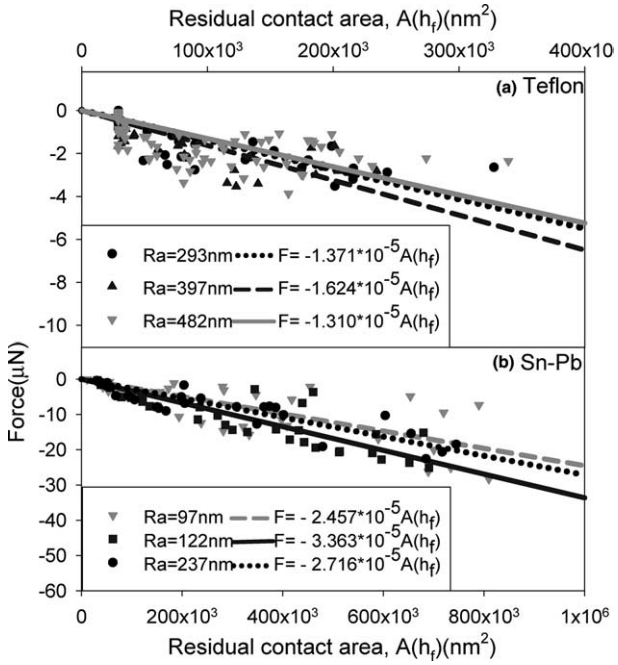

Fig. 9. The pull-off force as a linear function of the residual contact area (a) for the Teflon samples and (b) for the Sb–Pd samples.

4.4. Surface plastic work

After determining the values of F and f_s, we calculate the surface plastic work per project area, e_c, from Eq. (13) and list the calculated results in Table 1. As indicated in Table 1, the surface plastic work per project area is two or three orders higher in magnitude than the corresponding work of adhesion, thereby yielding an apparent surface stress two or three orders higher in magnitude than the thermodynamic surface stress, as indicated in Table 1. We may calculate the value of e_c with the use of Eq. (15) if the plastic flow pressure, p_0, is available. The plastic flow pressure can be estimated by the macrohardness, H_0. For example, Johnson [30] estimated it to be $p_0 \approx 0.39H_0$. The surface plastic work per project area, e_c, depends on the roughness, but the plastic flow pressure and the hardness at the infinite indentation depth are both independent of the roughness. As a direct consequence, the ratio of $p_0/H_0 = e_c/(V_pH_0)$ should be almost a constant regardless of the surface roughness. Table 1 indicates the ratios of $e_c/(V_pH_0)$ for the tested samples. As expected, the ratios of $e_c/(V_pH_0)$ are 0.27 and 0.22 for the Sn–Pd and the Teflon samples, respectively. The results indicate that the ratios for both materials are almost the same, which is expected from the theoretical model.

4.5. Critical depth, h_c

Zhang and Xu [26] proposed a critical contact depth, h_c,

$$h_c = \frac{(A^*)^2}{h^* - 2A^*} \quad \text{for the dislocation theory of plasticity if } h^* > 2A^*, \tag{18a}$$

$$h_c = \frac{(A^*)^2}{h^*} \quad \text{for the molecular theory of plasticity,} \tag{18b}$$

where $A^* = gf/H_0$. The surface term predominates in the region of $h < h_c$, while the bulk term predominates in $h > h_c$. However, for the dislocation theory of plasticity, the surface term will predominate over the entire region of the indentation depth if $h^* \leqslant 2A^*$. We calculate the critical depth for the tested samples. As indicated in Table 1, the critical depths are 144, 181, and 109 nm for the Teflon polymers polished with 9, 3, and 0.3 μm alumina, respectively, thereby indicating that the rougher the indented surface, the deeper the critical depth is. The results are consistent with the fitting process that the value of F is first determined at a shallow depth region where the surface effect predominates. However, the critical depths are 137, 27, and 6 nm for the Sn–Pd samples polished with 3, 1, and 0.05 μm alumina, respectively. The fitting results for the Sn–Pd sample polished with 3 μm alumina are approximately consistent with the fitting process, whereas the other two values are too small to be consistent with the fitting process when the value of F is extracted from fitting the data of depths less than 150 nm. As mentioned above, the fitting is not unique in the determination of the three parameters from the experimental data. Nevertheless, the consistent experimental results from the four samples verify the bearing ratio model, showing that plastic deformation at indented surfaces creates apparent surface stresses with very high values in magnitude in comparison with the thermodynamic surface stresses.

4.6. Fully plastic deformation of asperities

Zhao et al. [61] studied the elastic–plastic contact of rough surfaces. Their results indicate that for an asperity with a radius of R_{asp}, only elastic deformation occurs if $\omega < \omega_1$, where ω denotes the local interference and $\omega_1 = (3\pi KH/4E)^2 R_{asp}$ is the critical interference at the point of initial yielding, E is Young's modulus of the rough surface, H is the hardness of the material, and K is a dimensionless constant, which is the parameter, $e_c/(V_p H_0)$, listed in Table 1. Elastic–plastic deformation occurs if $\omega_1 < \omega < \omega_2$ and fully plastic deformation occurs if $\omega > \omega_2$, where $\omega_2 \geqslant 54\omega_1$. It is expected that the bearing ratio model is appropriate when fully plastic deformation occurs. The average Young's moduli of the experimental samples were estimated with a Poisson ratio of 0.3 from the unloading curves of the nanoindentation tests to be $E_{Sn-Pb} \approx 36.35 \pm 10.17$ GPa and $E_{Teflon} \approx 1.591 \pm 0.682$ GPa, respectively. The hardness and the value of $e_c/(V_p H_0)$, as listed in Table 1, are $H_{Sn-Pb} \approx 0.209$ GPa and $K = e_c/(V_p H_0) = 0.27$ for the Sn–Pb alloys and $H_{Teflon} \approx 0.036$ GPa and $K = e_c/(V_p H_0) = 0.22$ for the Teflon samples. Thus, we have $54\omega_1 = 0.000719 R_{asp}$ for the Sn–Pb alloys and $54\omega_1 = 0.00743 R_{asp}$ for the Teflon samples. The range of indentation loads was set from 0.2 to 9.9 mN in the tests on both the Teflon and Sn–Pd samples, which yielded indentation contact depths ranging from about 10 to about 450 nm for the Teflon samples and from about 5 to about 1500 nm for the Sn–Pd samples. To meet the criterion for fully plastic deformation, the values of R_{asp} should be smaller than 60,565 and 2,086,231 nm for the Teflon and Sn–Pd samples, respectively. The surface morphology measurements show that the values of R_{asp} are about 873 and 1317 nm for the Teflon and Sn–Pd samples, respectively, thereby indicating that the criterion for fully plastic deformation is satisfied and asperities on the indented rough surfaces of the Sn–Pb and Teflon samples must fully deform plastically.

5. Concluding remarks

The proposed bearing ratio model is able to assess quantitatively the degree of the plastic work done on a rough indented surface. The designed nanoindentation tests on both crystalline and amorphous materials with different surface roughnesses verify the proposed bearing ratio model. The experimental and theoretical results indicate that the rougher the indented surface is, the more the energy dissipated during the plastic deformation and the more significant the ISE will be. The apparent surface stress extracted from the nanoindentation tests is about two or three orders higher in magnitude than the thermodynamic surface energy of the same material. This apparent surface stress mainly represents the dissipation energy per project area due to the plastic deformation occurring at the indented surface.

Acknowledgements

This work was supported by an RGC grant (HKUST6016/02E) from the Research Grants Council of the Hong Kong Special Administrative Region, China and by an I^{2}MS Research Fund (I2MS01/02.EG10) from the Institute of Integrated Microsystems, Hong Kong University of Science and Technology. The authors thank Dr. Y.T. Cheng from GM, USA, and Dr. J.R. Li for useful discussion and constructive suggestions. T.-Y.Z. thanks the Croucher Foundation for the Croucher Senior Research Fellowship Award, which

gave him more research time by releasing him from teaching duties.

References

[1] Brinell JA. 2ième congres. Internationale Méthodes d'Essai, Paris; 1900.
[2] Wahlberg A. J Iron Steel Inst 1901;59:243.
[3] Mott BW. Micro-indentation hard testing. London: Butterworths; 1956.
[4] Bückle H. Metal Rev 1959;4:49.
[5] Pethica JB, Hutchings R, Oliver WC. Phil Mag 1983;48:593.
[6] Olive WC, Pharr GM. J Mater Res 1992;7:1564.
[7] Field JS, Swain MV. J Mater Res 1993;8:297.
[8] Cahn RW. Nature 1992;357:645.
[9] Lawn BR, Padture NP, Cai HD, Guiberteau F. Science 1994;263:1114.
[10] Li J, Van Vliet KJ, Zhu T, Yip S, Suresh S. Nature 2002;418:307.
[11] Dao M, Chollacoop N, Van Vliet KJ, Venkatesh TA, Suresh S. Acta Mater 2001;49:3899.
[12] Cheng YT, Cheng CM. Appl Phys Lett 1998;73:614.
[13] Gane N, Cox JM. Phil Mag 1970;22:881.
[14] Sangwal K. J Mater Sci 1989;24:1128.
[15] Weppelmann ER, Field JS, Swain MV. J Mater Res 1993;8:830.
[16] Cheng YT, Cheng CM. Phil Mag Lett 2001;81:9.
[17] Ma Q, Clark DR. J Mater Res 1995;10:853.
[18] Poole WJ, Ashby MF, Fleck NA. Scripta Mater 1996;34:559.
[19] McElhaney KW, Vlassak JJ, Nix WD. J Mater Res 1998;13:1300.
[20] Krell A, Schadlich S. Mater Sci Eng A 2001;307:172.
[21] Bull SJ, Page TF, Yoffe EH. Phil Mag Lett 1989;59:281.
[22] Li H, Ghosh A, Han YH, Bradt RC. J Mater Res 1993;8:1028.
[23] Gong JH, Miao HZ, Zhao Z, Guan ZD. Mater Sci Eng A 2001;303:179.
[24] Lim YY, Chaudhri MM. Phil Mag 1999;79:2927.
[25] Nix WD, Gao H. J Mech Phys Sol 1998;46:411.
[26] Zhang TY, Xu WH. J Mater Res 2002;17:1715.
[27] Bradby JE, Williams JS, Wong-Leung J, Swain MV, Munroe P. J Mater Res 2001;16:1500.
[28] Ashby MF. Phil Mag 1970;21:399.
[29] Stelmashenko NA, Walls MG, Brown LM, Milman YV. Acta Metal Mater 1993;41:2855.
[30] Johnson KL. Contact mechanics. Cambridge: Cambridge University Press; 1985.
[31] Fischer-Cripps AC. Introduction to contact mechanics. New York: Springer; 2000.
[32] Yu WP, Blanchard JP. J Mater Res 1996;11:1358.
[33] Gerberich WW, Tymiak NI, Grunlan JC, Horstemeyer MF, Baskes MI. J Appl Mech, T ASME 2002;69:433.
[34] Tymiak NI, Kramer DE, Bahr DF, Wyrobek TJ, Gerberich WW. Acta Mater 2001;49:1023.
[35] Gerberich WW, Kramer DE, Tymiak NI, Volinsky AA, Bahr DF, Kriese MD. Acta Mater 1999;47:4115.
[36] Swadener JG, George EP, Pharr GM. J Mech Phys Sol 2002;48:681.
[37] Xue Z, Huang Y, Hwang KC, Li M. J Eng Mater Tech 2002;124:371.
[38] Swadener JG, Misra A, Hoagland RG, Nastasi M. Scripta Mater 2002;47:343.
[39] Elmustafa AA, Stone DS. Acta Mater 2002;50:3641.
[40] Elmustafa AA, Stone DS. J Mech Phys Sol 2003;51:357.
[41] Qiu X, Huang Y, Nix WD, Hwang KC, Gao H. Acta Mater 2001;49:3949.
[42] Lam DCC, Chong ACM. J Mater Res 1999;14:3784.
[43] Chong ACM, Lam DCC. J Mater Res 1999;14:4103.
[44] McColm IJ. Ceramic hardness. New York: Plenum; 1999.
[45] Liu Y, Ngan AHW. Scripta Mater 2001;44:237.
[46] Quinn JB, Quinn GD. J Mater Sci 1997;32:331.
[47] Bernhardt EO. Z Metallkde 1941;33:135.
[48] Fröhlich F, Grau P, Grellmann W. Physica Status Solidi A 1977;42:79.
[49] Hirao K, Tomozawa M. J Am Ceram Soc 1987;70:497.
[50] Swain MV, Wittling M. Surf Coatings Technol 1995;77:528.
[51] Bobji MS, Biswas SK. J Mater Res 1998;13:3227.
[52] Gao YX, Fan H. J Mater Sci 2002;37:4493.
[53] Chang WR, Etsion I, Bogy DB. J Tribol T ASME 1987;109:257.
[54] Abbott EJ, Firestone FA. Mech Eng 1933;55:569.
[55] Pullen J, Williamson JBP. Proc R Soc Lond A 1972;327:159.
[56] Derjaguin BV, Muller VM, Toporov YP. J Colloid Interf Sci 1975;53:301.
[57] Johnson KL, Greenwood JA. J Colloid Interf Sci 1997;192:326.
[58] Nakamoto S, Tashiro K, Matsumoto A. J Polym Sci 2003;41:444.
[59] Smith GS, Tadmor EB, Kaxiras E. Phys Rev Lett 2000;84:1260.
[60] Okamatsu T, Yasuda Y, Ochi M. J Appl Polym Sci 2001;80:1920.
[61] Zhao Y, Maietta DM, Chang L. J Tribol T ASME 2000;122:86.